



Sparse Coding-enabled Low-fluence Multi-parametric Photoacoustic Microscopy

Zhuoying Wang, Yifeng Zhou, and Song Hu

Abstract—Uniquely capable of simultaneous imaging of the hemoglobin concentration, blood oxygenation, and flow speed at the microvascular level in vivo, multi-parametric photoacoustic microscopy (PAM) has shown considerable impact in biomedicine. However, the multi-parametric PAM acquisition requires dense sampling and thus a high laser pulse repetition rate (up to MHz), which sets a strict limit on the applicable pulse energy due to safety considerations. A similar limitation is shared by high-speed PAM, which also uses lasers with high pulse repetition rates. To achieve high quantitative accuracy besides good structural visualization at low levels of laser fluence in PAM, we have developed a new, sparse coding-based two-step denoising technique. In the setting of intravital brain imaging, we demonstrated that this unsupervised learning approach enabled the reduction of the laser fluence in PAM by 5 times without compromise of the image quality (structural similarity index measure or SSIM: >0.92) and the quantitative accuracy (errors: <4.9%). Offering a significant relaxation in the requirement of PAM on laser fluence while maintaining the quality of structural imaging and accuracy of quantitative measurements, this sparse coding-based approach is expected to facilitate the application and clinical translation of multi-parametric PAM and high-speed PAM, which have a tight photon budget due to either safety considerations or laser source limitations.

Index Terms—Photoacoustic microscopy, low-fluence functional imaging, quantitative imaging, sparse coding, denoising

I. INTRODUCTION

HIGHLY sensitive to the optical absorption-based molecular contrast, photoacoustic microscopy (PAM) has attracted considerable attention since being introduced to the biomedical community as an intravital imaging technique [1]. Capitalizing on the light absorption of hemoglobin, PAM enables label-free, comprehensive characterization of microvascular structure and function *in vivo* [2], [3]. Providing new functional and oxygenmetabolic insights into various physiological and pathological processes, PAM has found broad applications in both basic and translational biomedicine [4], [5].

Recent advances in the multi-parametric PAM [6], [7], which enables simultaneous imaging of the hemoglobin concentration (C_{Hb}), oxygen saturation of hemoglobin (sO₂), and blood flow at the microscopic level, further expand its promise. However, quantification of C_{Hb} and blood flow relies on dense sampling,

which requires a high laser pulse repetition rate (PRR) [8], [9]. Moreover, recent efforts on improving the speed of PAM boost the use of lasers with high PRRs (up to MHz) [10], [11], which leads to increased photon energy deposition in biological tissue per unit time and thus limits the applicable pulse energy due to laser safety considerations [12]. Besides safety concerns, high laser fluence may cause the saturation of optical absorption and thus inaccurate measurement of sO₂ [13].

Although imperative, achieving high structural image quality and quantitative accuracy with low-fluence excitation remains a challenge. At low-fluence levels, the signals generated by the microvasculature are comparable to the noise of PAM systems, resulting in a low signal-to-noise ratio (SNR) that is inadequate for microvascular visualization [14]. Even if some microvessels remain visible under low-fluence excitation, the reduced SNR causes errors in functional measurements as shown by us before [15]. To address this challenge, different techniques have been developed/adopted to improve the quality of low-fluence photoacoustic images [16]–[21], among which sparse coding has shown strong promise for denoising and artifact removal.

Widely used in computer vision and image processing [22]— [24], sparse coding is an unsupervised learning method seeking to represent the image data with a sparse, linear combination of dictionary atoms [25]. Given that unfeatured noise patterns are less correlated and have less sparse representations than signals, sparse coding can differentiate them and has been applied by us and others to remove noise and artifacts in the structural images acquired by PAM [19], [21]. Although demonstrating marked improvement in the SNR of trunk vessels, these efforts have not led to appreciable enhancement in microvascular visualization. More importantly, most of the current studies have been limited to improving the structural image quality—leaving quantitative imaging of the microvascular function unattended. Recently, a deep learning-based technique was developed for denoising the maximum amplitude projection (MAP) image in PAM [26]. Although quantitative imaging of the sO₂ is achieved with 50% reduction in the laser pulse energy, this method cannot improve the quantification of blood flow, which requires direct analysis of depth-resolved A-lines.

In this paper, we present a new two-step sparse coding-based image processing technique that enables significantly enhanced microvascular visualization and highly accurate quantification of microvascular functions in multi-parametric PAM with low-

Manuscript received xxx xx, 2021; accepted xxx xx, 2021. Date of the publication xxx xx, 2021; date of current version xxx xx, 2021. This work was supported in part by the National Institutes of Health (NS099261) and the National Science Foundation (2023988). (Corresponding author: Song Hu.)

The authors are with the Department of Biomedical Engineering, McKelvey School of Engineering, Washington University in St. Louis, MO 63130 USA (email: zhuoying.wang@wustl.edu; yifengzhou@wustl.edu; songhu@wustl.edu).

fluence excitation. After testing the feasibility of this technique in a fiber phantom, we demonstrated its utility by imaging the microvascular structure, C_{Hb}, sO₂, and blood flow speed in the same mouse brain at normal (100 nJ pulse energy) and reduced (20, 10, and 5 nJ) fluence levels. Comparison of the structural and functional images before and after the two-step denoising against those acquired with the normal laser fluence provides a comprehensive assessment of its performance *in vivo*.

II. METHODS

A. K-SVD-based Sparse Coding

Under the sparse assumption, the image data admits a sparse decomposition over an overcomplete dictionary [24]. The goal of sparse coding is to describe the data with a trained dictionary and a sparse coefficient matrix [27]. In this work, we use the K-SVD algorithm to train the dictionaries because of its efficiency and simplicity [28].

Given a noisy image y, the goal is to define an overcomplete dictionary D and identify a sparse coefficient matrix x, which together best represent a noise-free version of the image

$$\widehat{\mathbf{y}} \approx \mathbf{D}\mathbf{x}.\tag{1}$$

The process can be described as an optimization problem

$$(\boldsymbol{x}, \boldsymbol{D}) = \underset{\boldsymbol{x}}{\operatorname{argmin}} \|\boldsymbol{x}\|_{0} \text{, s. t. } \|\boldsymbol{y} - \boldsymbol{D}\boldsymbol{x}\|_{2}^{2} \le \epsilon, \tag{2}$$

in which ϵ is related to the noise in the raw image y. Since x is sparse, this problem can be rewritten into

$$(x, D) = \underset{x \, D}{\operatorname{argmin}} \|y - Dx\|_{2}^{2}, \text{ s. t. } \|x\|_{0} \le S,$$
 (3)

where S is the desired sparsity (*i.e.*, the largest number of non-zero entries of x).

When sparse coding is applied to process a large image, the raw image is usually divided into small patches. In this case, the optimization problem can be solved for each patch as

$$(x_i, \mathbf{D}) = \underset{x_i, \mathbf{D}}{\operatorname{argmin}} \|\mathbf{R}_i \mathbf{y} - \mathbf{D} \mathbf{x}_i\|_2^2 \text{, s. t. } \|\mathbf{x}_i\|_0 \le S, \quad (4)$$

where i denotes the patch index, and operator R_i extracts patch

i from the original large image y.

To solve this problem, first, the K-SVD algorithm initializes the dictionary and coefficient matrix as \hat{D} and \hat{x}_i , respectively. Specifically, the dictionary is initialized by a randomly valued matrix and the coefficient matrix is approximated by using the orthogonal matching pursuit (OMP) algorithm [29]. With this, the residual of an arbitrary column c in \hat{D} can be computed as

 $e_i^c = \mathbf{R}_i \mathbf{y} - \sum_{k \neq c} \mathbf{d}^k \mathbf{x}_i^k = \mathbf{R}_i \mathbf{y} - \widehat{\mathbf{D}} \widehat{\mathbf{x}}_i + \mathbf{d}^c \mathbf{x}_i^c$, $i \in P_c$, (5) where \mathbf{d}^k is the kth column of $\widehat{\mathbf{D}}$, \mathbf{x}_i^k is the coefficient in kth row of $\widehat{\mathbf{x}}_i$, respectively, and P_c is the set of patches that use atom \mathbf{d}^c : $P_c = \{i | \mathbf{x}_i^c \neq \mathbf{0}\}$. Traversing all columns leads to a residual matrix

$$\boldsymbol{E}_c = \{e_i^c\}, \ i \in P_c. \tag{6}$$

Then, the dictionary \widehat{D} is updated by minimizing the difference between $R_i y$ and $\widehat{D} \widehat{x}_i$, which can be solved by approximating E_c with a rank-one matrix via the singular value decomposition as

$$\boldsymbol{E}_{c} = \boldsymbol{U}\boldsymbol{\Sigma}\boldsymbol{V}^{T},\tag{7}$$

where Σ is the diagonal singular values matrix, and U and V are the left and right singular vectors, respectively. Column d^c of the updated dictionary is the first column of U. The coefficient x_i^c is calculated by multiplying the first column of V by $\Sigma(1,1)$. After all columns are updated, a new coefficient matrix can be generated using the OMP algorithm. Iterative updates of both the dictionary and the coefficient matrix eventually solve the optimization problem and generate a noise-free image.

B. Two-step Denoising Strategy

Combining two-dimensional (2-D) transverse scan and timeresolved ultrasonic detection, PAM produces three-dimensional (3-D) image sets, consisting of a series of cross-sectional scans (*i.e.*, B-scans) acquired at different tissue locations. Due to the considerable anisotropy in spatial resolution (lateral resolution: a few μ m; axial resolution: tens of μ m), PAM images are often presented in 2-D by projecting the maximum amplitude of each A-line along the axial/depth direction (*i.e.*, MAP images).

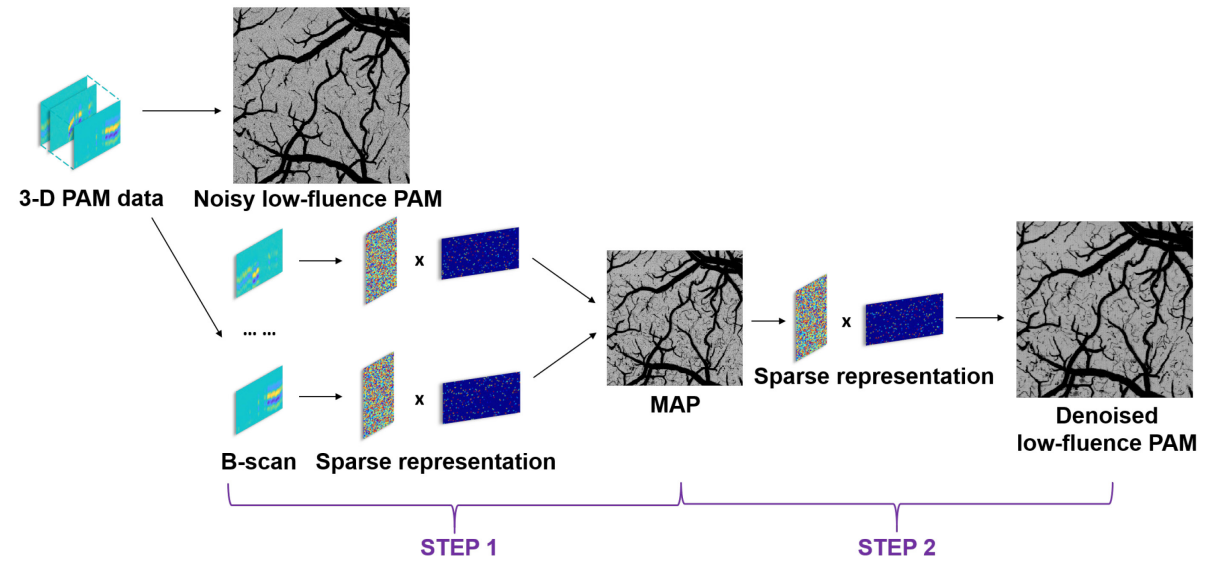


Fig. 1. Flow diagram of two-step sparse coding-based denoising

To fully exploit the 3-D imaging nature of PAM, we propose a two-step sparse coding-based denoising strategy. As shown in Fig. 1, sparse coding is applied first to each raw B-scan acquired by low-fluence PAM and then to the MAP image composited by the denoised B-scans. The two steps are complementary. In the first step, sparse coding can effectively separate the vascular signals from random noise in individual A-lines of the B-scan because the noise is much less sparse compared to the signals. Removing the noise while preserving the weak microvascular signals in A-lines can significantly enhance the visualization of microvessels. However, the noise and possible electromagnetic interference (EMI) that present in patterns similar to that of the spike-like vascular signal in A-lines remain largely unaffected. In the second step, the MAP image, where the vascular pattern is distinct from those of the noise and possible EMI, is sparsely coded by the K-SVD algorithm for separation and removal of the residual non-vessel components. Combining these two steps of denoising results in a near-background-free vascular image. The same K-SVD algorithm is applied in both steps for sparse coding. Note that no other signal processing is involved besides the two-step sparse coding-based denoising.

In this denoising technique, there are four key parameters—dictionary atom size, desired sparsity, patch size, and iteration number. Proper selection of these hyperparameters is essential because of the tradeoff between removing noise and preserving signal. For example, smaller desired sparsity allows better noise suppression, but an excessively small desired sparsity may lead to changes in the amplitude or profile of vascular signals and affect quantitative measurements. Also, larger atom size better preserves vascular signal for quantitative measurements, but an overly large atom size may compromise the efficacy of noise removal. Moreover, the computational cost is a practical factor to consider when selecting the hyperparameters. Thus, the patch size and iteration number should not be too large while ensuring convergence.

Balancing the denoising performance, quantitative accuracy, and computational cost, we have determined the parameters for the two-step sparse coding-based technique as follows:

Step 1. atom size = 50, desired sparsity = 3, patch size = 100×1 , iteration = 50.

Step 2. atom size = 50, desired sparsity = 7, patch size = 250×1 , iteration = 80.

C. Experimental Setup

A self-developed multi-parametric PAM system was used in this study. As shown in Fig. 2, the 532-nm output from a nanosecond pulsed laser (GLPM-10, IPG Photonics) is launched into an acousto-optic modulator (AOM, AOMO 3080-122, Crystal Technology) for pulse-by-pulse wavelength conversion. When the AOM is off, the pulsed light undergoes no diffraction and is coupled into a polarization-maintaining single-mode fiber (PM-SMF, HB450-SC, Fibercore), in which the light wavelength is red-shift due to the stimulated Raman scattering effect [30]. The fiber output then passes a bandpass filter (BPF, CT560/10bp, Chroma) to select out the 558-nm component. When the AOM is on, ~60% of the 532-nm light is diffracted into a different optical path (*i.e.*, 1st-order diffraction), where it experiences no

wavelength conversion. The undiffracted (i.e., 0th-order) light, accounting for ~40% of the energy, is insufficient to generate nonlinear Raman scattering and thus is removed by the BPF. As a result, the AOM switches the wavelength of the laser pulses between 532 and 558 nm. The two optical paths are combined by a dichroic mirror (DM, FF538-FDi01, Semrock). The energy of each laser pulse is modulated by an electro-optic modulator (EOM, 350-80, Conoptics) combined with a polarizing beamsplitter (PBS, PBS121, Thorlabs). To compensate for possible laser fluctuation, ~5% of the laser light is tapped off by a beam sampler (BS, BSF10-A, Thorlabs) and monitored by a highspeed photodiode (PD, PDA36A2 Thorlabs). An objective lens (OL, AC254-050-A, Thorlabs) focuses the beam onto the object to be imaged through a ring-shaped ultrasonic transducer (UT, inner diameter: 1.1 mm; outer diameter: 3.0 mm; focal length: 4.4 mm; center frequency: 40 MHz; 6-dB bandwidth: 69%). For acoustic coupling, the transducer is submerged into a water tank (WT) and a thin layer of ultrasound gel (Aquasonic CLEAR, Parker Laboratories) is applied between the target and the tank bottom. A correction lens (CL, LA1207-A, Thorlabs) is used to compensate for the optical aberration induced at the interface of the ambient air and water.

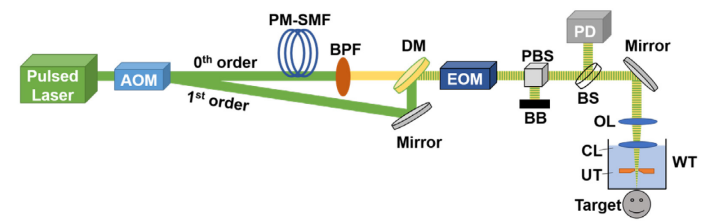


Fig. 2. Schematic of multi-parametric PAM. AOM: acousto-optic modulator, PM-SMF: polarization-maintaining single-mode fiber; BPF: bandpass filter; DM: dichroic mirror; EOM: electro-optic modulator, PBS: polarizing beamsplitter, BB: beam block, BS: beam sampler, PD: photodiode, OL: objective lens, CL: correction lens, UT: ultrasound transducer, WT: water tank.

By adjusting the voltage applied to the EOM, the laser pulse energy on the target is altered between 5, 1, 0.5, and 0.25 nJ for phantom imaging and 100, 20, 10, and 5 nJ for in vivo imaging, allowing simultaneous PAM of the same region of interest at different fluence levels. For in vivo experiments, the laser safety standards defined by the American National Standards Institute (ANSI) is considered when determining the laser fluence. The highest fluence levels (in the case of 100-nJ laser pulses) are 19.7 mJ/cm² (532 nm) and 18.0 mJ/cm² (558 nm) at the surface of the mouse brain (beam waist: 1.75 μm, focal depth: 130 μm), which are within the ANSI limit (i.e., 20 mJ/cm²). For phantom imaging, the fluence is set at a much lower level because carbon fibers generate much stronger photoacoustic signals compared to microvessels in the mouse brain. Specifically, we used 5 nJ as normal fluence and 20%, 10% and 5% of it as low fluences (i.e., 1, 0.5, and 0.25 nJ), keeping the same ratio as the in vivo imaging to better benchmark the performance of our denoising method. Structural images of the carbon fibers and cerebral vasculature are generated by Hilbert transform and maximum amplitude projection of the depth-resolved A-lines, and C_{Hb}, sO₂, and blood flow images of the cerebral vasculature are

generated by the statistical, spectroscopic, and correlation analyses, respectively [8].

The phantom used in this study was randomly placed carbon fibers (average diameter: ~6 μm). The *in vivo* experiment was performed in the brain of a CD-1 mouse (male, 12 weeks old, Charles River Laboratories) through a cranial window. During the imaging experiment, the animal was anesthetized with 1.5% isoflurane, and the body temperature was kept at 37°C using a temperature-controlled heating pad (Cole-Parmer, EW-89802-52 and Omega, SRFG-303/10). All procedures were carried out in conformity with the laboratory animal protocol approved by the Institutional Animal Care and Use Committee (IACUC) at Washington University in St. Louis.

In this work, all data were processed in MATLAB (R2019b, MathWorks) using a personal computer (Intel i7-7700 CPU @ 3.60GHz). For the *in vivo* dataset, in the first step, 450 B-scan frames (128×7500 pixels each) were processed sequentially at a speed of 24 seconds/B-scan. In the second step, it took ~300 seconds to process one MAP image (450×7500 pixels). The total runtime of the denoising algorithm was ~3 hours without paralleling computation.

D. Quantitative Assessment of Denoising Performance

To quantitively assess the performance of the sparse codingbased two-step denoising technique, multiple key parameters, including the SNR, contrast-to-noise ratio (CNR) and structural similarity index measure (SSIM), are assessed and compared.

The SNR is defined as [31]

$$SNR = \bar{I}/\sigma_n, \tag{8}$$

where \bar{I} is the average amplitude of the vascular signal, and σ_n is the standard deviation of the amplitude of background noise.

The CNR is defined as [31]

$$CNR = (\bar{I} - \bar{I}_n)/\sigma_n, \tag{9}$$

where $\overline{I_n}$ is the average amplitude of the background.

The SSIM, a quantitative measure of the similarity between two images, is defined as [32]

$$SSIM(x,y) = l^{\alpha}(x,y)c^{\beta}(x,y)s^{\gamma}(x,y), \tag{10}$$

in which l(x, y), c(x, y), and s(x, y) respectively measure the differences between the luminance, contrast, and structure of the two images, and α , β , and γ are three constants. The SSIM map and average SSIM value of the result images are quantified against the reference images acquired with the normal fluence (*i.e.*, 5 nJ or 100 nJ). By selecting the default value of 1 for α , β , and γ , a larger SSIM value indicates higher similarity. Note that since our PAM can simultaneously acquire multiple images at different fluence levels (*i.e.*, 5, 1, 0.5, and 0.25 nJ or 100, 20, 10, and 5 nJ), no image registration is needed prior to the SSIM calculation.

III. RESULTS

First, we demonstrated the feasibility of the two-step sparse coding-based denoising technique in a carbon fiber phantom by processing and comparing the images acquired at normal (pulse energy: 5 nJ) and low fluence levels (1, 0.5, and 0.25 nJ).

As shown in Fig. 3a, the raw image of the phantom acquired with 20% of the normal fluence (*i.e.*, 1 nJ) shows considerable noise. Sparse coding-based denoising of the B-scans (*i.e.*, Step 1) improves the visualization of carbon fibers by reducing the noise in individual A-lines (as shown in Fig. 4a). However, the noise and possible EMI that have signal-like patterns in A-lines, remain largely unremoved (indicated by black arrows in Fig.

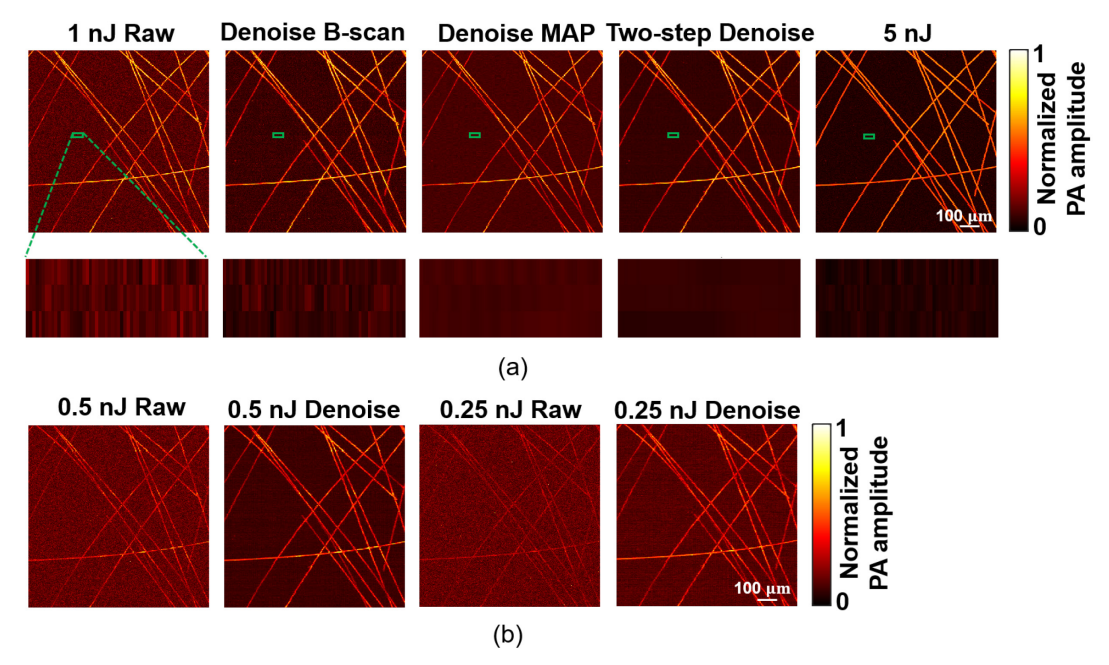


Fig. 3. Two-step denoising of carbon fiber images acquired by low-fluence PAM. (a) Step-by-step illustration of the performance of two-step denoising on images acquired with 20% of normal fluence. First row: low-fluence (*i.e.*, 1 nJ pulse energy) PAM images of randomly distributed carbon fibers before denoising, after B-scan denoising alone, MAP denoising alone, and two-step denoising, as well as the reference image acquired with normal fluence (*i.e.*, 5 nJ). Second row: Close-up views of non-fiber background. (b) Illustration of the denoising performance in images acquired with 10% and 5% of normal fluence (*i.e.*, 0.5 nJ and 0.25 nJ, respectively) through side-by-side comparison of the low-fluence images before and after two-step denoising. PA: photoacoustic.

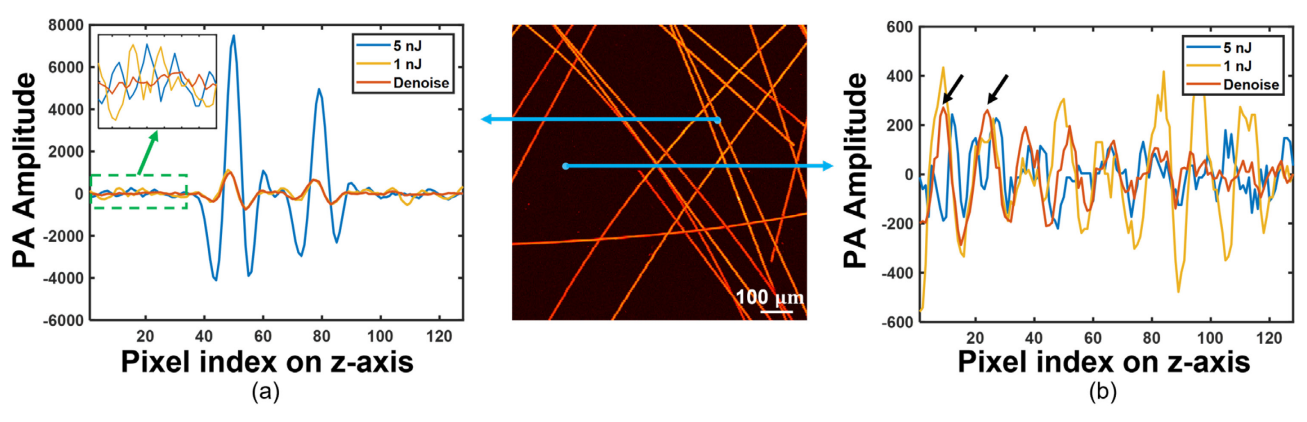


Fig. 4. Illustration of the performance of B-scan denoising on low-fluence PAM of the carbon fiber phantom. (a) Effective suppression of random noise in a representative A-line containing the carbon fiber signal. (b) Ineffective suppression of noise with signal-like patterns (indicated by the black arrows) in a representative A-line of the non-fiber background. The A-line signal is converted to a bipolar form by subtracting its mean.

4b) and present as background fluctuation in the MAP image (the second row of Fig. 3a). By contrast, directly denoising the MAP image with sparse coding (*i.e.*, Step 2) significantly suppresses the background fluctuation. However, the average amplitude of the background remains high, which hinders the enhancement of the image contrast, thus impedes improvement of microvascular visibility. Combining the two steps yields the best performance and generates a denoised image, whose quality is comparable to that acquired with the normal fluence (*i.e.*, 5 nJ). Further testing the denoising technique in carbon fiber images acquired at 10% and 5% of the normal fluence (*i.e.*, 0.5 and 0.25 nJ), which are even noisier and have poor visualization of the fibers, shows that the two-step denoising significantly improves the image quality (Fig. 3b).

To benchmark the performance of the denoising technique, the key parameters of the raw and denoised images, including the SNR, CNR, and SSIM (against the reference image acquired with 5 nJ pulse energy), are quantified and compared. As shown in Table I, the two-step denoising technique improves the SNR and CNR of the low-fluence images acquired with 20%, 10%, and 5% of the normal fluence by 4.3-6.1 times and 7.2-8.8 times, respectively, whereas the SSIM is increased by 0.23-0.47. The lower the laser fluence, the larger the improvements in the CNR and SSIM. Moreover, step-by-step analysis of the performance of the two-step denoising technique on the image acquired with 20% of the normal fluence shows that denoising the B-scans (i.e., Step 1) results in a larger improvement in the SSIM compared to directly denoising the MAP image (i.e., Step 2), indicating a better visualization of the carbon fiber structure. By contrast, directly denoising the MAP image leads to a larger improvement of the SNR and CNR, suggesting a more effective suppression of background noise.

Then, we examined the utility of the two-step sparse coding-based denoising for enhancing the microvascular visualization and hemodynamic quantification accuracy of low-fluence PAM in an intravital brain imaging setting. Specifically, the brain of a live CD-1 mouse was concurrently imaged at normal (pulse energy: 100 nJ) and low fluence levels (20, 10, and 5 nJ). The performance of the two-step denoising technique in low-fluence PAM was benchmarked against the images acquired under the normal fluence condition.

At 20% of the normal laser fluence (i.e., 20 nJ pulse energy), the two-step approach demonstrated excellent performance. As shown in Fig. 5a, the raw structural image acquired with 20 nJ laser pulses shows sparsely distributed microvessels, along with considerable non-vessel background. The sparse coding-based denoising of the B-scan (i.e., Step 1) significantly reduces the random noise in individual A-lines. Such noise removal in Alines containing weak microvascular signals (as shown in Fig. 6a, where the noise indicated by the red arrow is comparable to the microvascular signal indicated by the green arrow) results in a much improved visualization of the microvessels that are barely visible in the raw image (blue arrows in Fig. 5a). However, the background in the B-scan denoised image still contains dotted patterns, likely due to ineffective suppression of the signal-like noise and/or EMI in A-lines (indicated by black arrow in Fig. 6b). Directly applying sparse coding to denoise the raw MAP image (i.e., Step 2 only) significantly reduces the fluctuation of the background noise but does not lead to significant improvement of microvascular visualization. Combining the two steps results in a more complete noise removal and a high-quality image of the microvascular structure—approaching that acquired with the normal fluence (i.e., 100 nJ).

TABLE I
STEP-BY-STEP ANALYSIS OF THE EFFECTS OF TWO-STEP DENOISING ON SNR, CNR, AND SSIM AT DIFFERENT FLUENCE LEVELS IN PHANTOM

Metric	5 nJ	1 nJ				0	5 nJ	0.25 nJ	
		Raw	Denoise	Denoise	Two-step	Raw	Two-step	Raw	Two-step
			B-scan	MAP	Denoise	Naw	Denoise		Denoise
SNR	103.33	20.87	30.49	66.04	127.06	10.42	60.63	7.35	31.33
CNR	98.22	15.72	27.20	49.94	113.47	5.29	46.47	2.18	19.23
SSIM	1	0.66	0.82	0.74	0.89	0.40	0.83	0.24	0.71

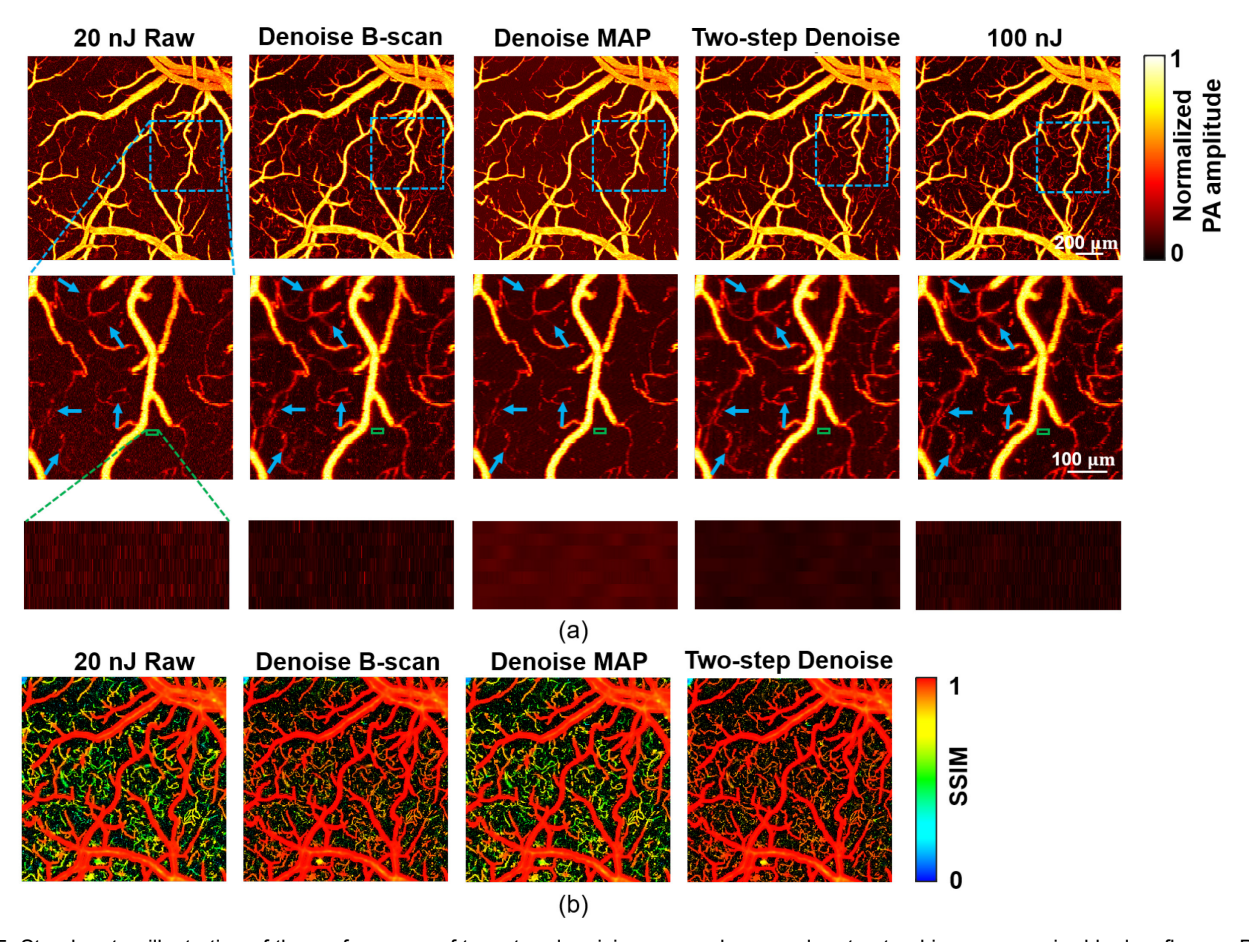


Fig. 5. Step-by-step illustration of the performance of two-step denoising on cerebrovascular structural images acquired by low-fluence PAM in the live mouse. First row: low-fluence (*i.e.*, 20 nJ pulse energy) images of the cerebral vasculature before denoising (raw), after B-scan denoising alone, MAP denoising alone, and two-step denoising, as well as the reference image acquired with normal fluence (*i.e.*, 100 nJ). Second row: Close-up views of the blue boxed region, showing the improvement of microvascular visualization (indicated by blue arrows). Third row: Close-up views of the green boxed region, showing the suppression of noise fluctuation in non-vessel background. (b) Pseudocolor-coded maps of the SSIM between the low-fluence PAM images (before and after denoising) and the reference image acquired with normal fluence. PA: photoacoustic.

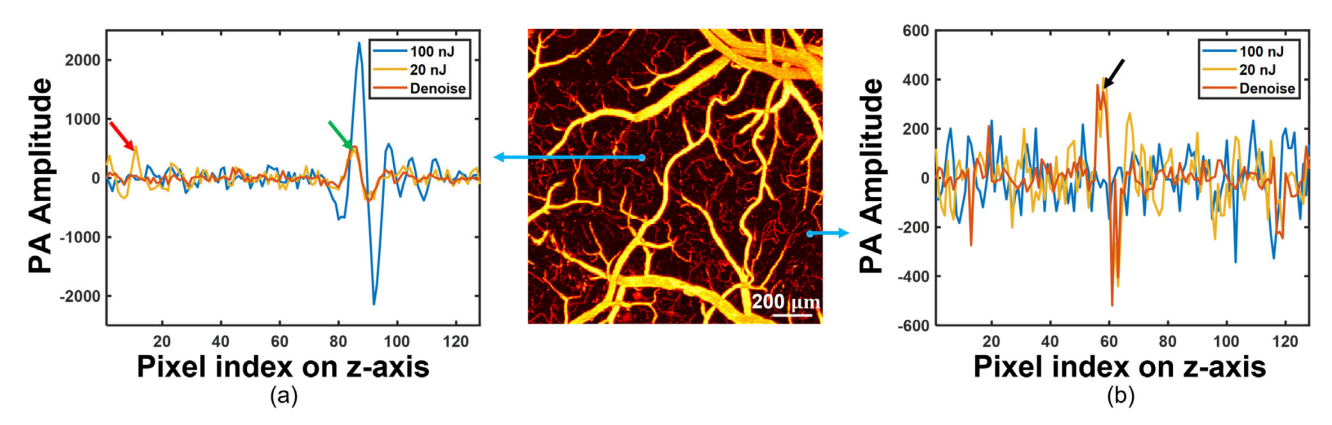


Fig. 6. Illustration of the performance of B-scan denoising on low-fluence PAM of the mouse cerebral vasculature *in vivo*. (a) Effective suppression of noise (indicated by the red arrow) with an amplitude comparable to that of the microvascular signal (indicated by the green arrow), in a representative A-line. (b) Ineffective suppression of noise with signal-like patterns (indicated by the black arrow) in a representative A-line of the non-vessel background. The A-line signal is converted to a bipolar form by subtracting its mean.

Quantitative comparison of the SNR, CNR, and SSIM values of the raw and denoised images acquired with 20 nJ laser pulses against the parameters of the image acquired with 100 nJ pulses in Table II shows three key observations. (1) The two-step denoising improves the SNR of the large vessels and microvessels by 4.9 and 5.7 times, respectively, and the CNR by 6.0 and 8.0 times, respectively. In addition, the two-step denoising improves the SSIM between the 20-nJ image and the reference image acquired at 100 nJ to 0.92, which indicates a high similarity (also shown in Fig. 5b). (2) The improvement in microvascular visualization is predominantly attributed to the B-scan denoising but not the MAP image denoising. Denoising the MAP image does not result in an appreciable increase in the microvascular SSIM (from 0.77 to 0.80). By contrast, denoising the B-scan leads to a significant increase in the microvascular

SSIM (from 0.77 to 0.93). (3) Denoising the MAP image plays a dominant role in enhancing the SNR and CNR by suppressing the fluctuation of background noise.

Besides the enhancement of microvascular visualization, the two-step approach also improves the accuracy of hemodynamic quantification at low-fluence levels. After denoising, the multiparametric images acquired with 20 nJ pulses show C_{Hb} , sO_2 , and flow speed values similar to those in the reference images acquired using 100 nJ pulses, as respectively shown in Fig. 7a–c. The denoising-induced improvement in quantitative accuracy is benchmarked by the SSIM between the low-fluence images (before and after denoising) and reference images, as shown in Table III. For the C_{Hb} measurement, the denoising technique improves the SSIM from 0.74 to 0.97 in large vessels and from 0.69 to 0.97 in microvessels. For the sO_2 measurement, the

STEP-BY-STEP ANALYSIS OF THE EFFECTS OF TWO-STEP DENOISING ON SNR, CNR, AND SSIM AT DIFFERENT FLUENCE LEVELS IN VIVO

Metric	Region ^a	100 nJ	20 nJ				10 nJ		5 nJ	
			Raw	Denoise B-scan	Denoise MAP	Two-step Denoise	Raw	Two-step Denoise	Raw	Two-step Denoise
SNR	Large vessel	196.57	44.75	80.04	157.67	253.03	25.35	134.96	15.35	63.94
	Microvessel	33.54	7.18	11.31	24.99	35.35	4.85	18.73	4.05	9.88
CNR	Large vessel	192.41	41.09	77.64	145.04	245.70	21.70	127.56	11.71	57.74
	Microvessel	29.38	3.52	8.91	12.36	28.02	1.20	11.33	0.41	3.68
	Large vessel		0.97	0.98	0.97	0.98	0.94	0.97	0.89	0.95
SSIM	Microvessel	1	0.77	0.93	0.80	0.94	0.53	0.83	0.34	0.65
	Whole image		0.73	0.87	0.78	0.92	0.58	0.83	0.46	0.68

^aDifferential analysis on large vessels and microvessels is enabled by vessel segmentation shown in Supplementary Materials.

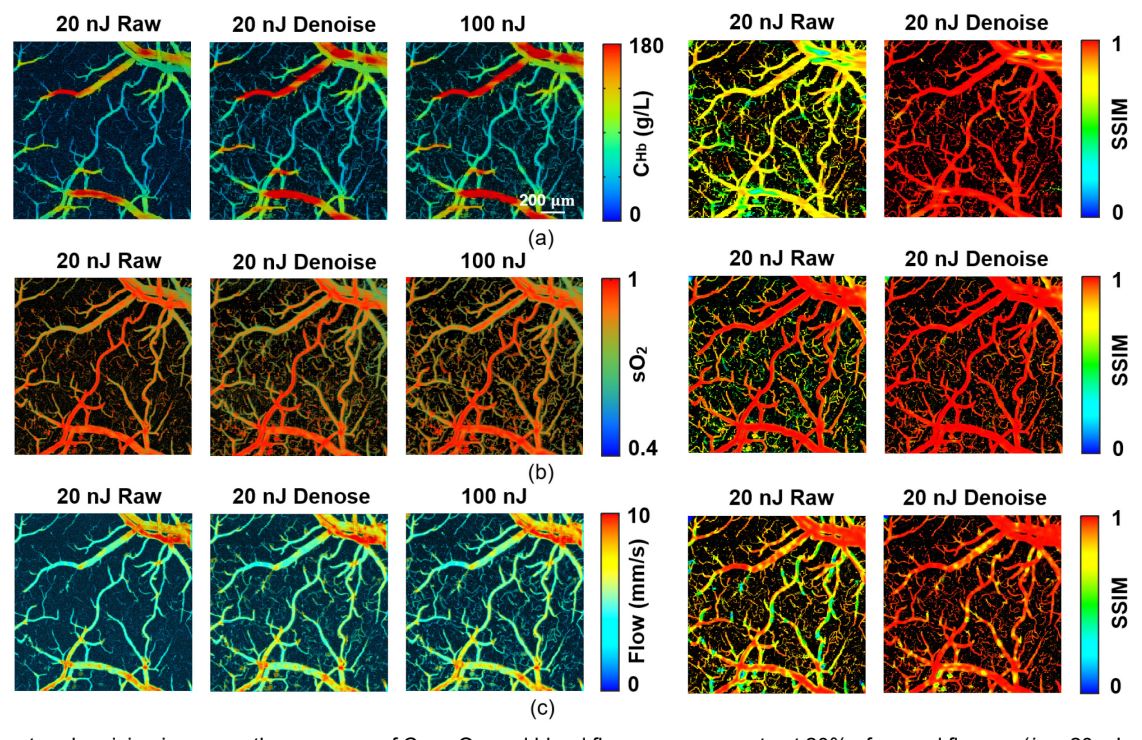


Fig. 7. Two-step denoising improves the accuracy of C_{Hb} , sO_2 , and blood flow measurements at 20% of normal fluence (*i.e.*, 20 nJ pulse energy). (a) Low-fluence C_{Hb} images before and after denoising, as well as the reference image acquired with normal fluence (*i.e.*, 100 nJ). Pseudocolor-coded maps of the SSIM between low-fluence C_{Hb} images (before and after denoising) and the reference image. (b) Low-fluence sO_2 images before and after denoising, as well as the reference image acquired with normal fluence. Pseudocolor-coded maps of the SSIM between low-fluence sO_2 images (before and after denoising) and the reference image. (c) Low-fluence blood flow images before and after denoising, as well as the reference image acquired with normal fluence. Pseudocolor-coded maps of the SSIM between low-fluence blood flow images (before and after denoising) and the reference image.

TABLE III
SSIM BETWEEN CEREBROVASCULAR FUNCTION MEASURED AT LOW FLUENCES (BEFORE AND AFTER DENOISING) AND NORMAL FLUENCE

Damamatana	Danian a	100 nJ	20 nJ		10 nJ		5 nJ	
Parameters	Region ^a		Raw	Denoise	Raw	Denoise	Raw	Denoise
C_{Hb}	Large vessel	1	0.74	0.97	0.49	0.89	0.25	0.67
	Microvessel	1	0.69	0.97	0.39	0.87	0.21	0.58
${ m sO}_2$	Large vessel	1	0.97	0.98	0.94	0.97	0.92	0.94
	Microvessel	1	0.74	0.93	0.59	0.83	0.48	0.69
Flow	Large vessel	1	0.83	0.94	0.80	0.91	0.73	0.88
	Microvessel	1	0.78	0.93	0.71	0.87	0.67	0.78

^aSame as Table II.

denoising not only maintains the high accuracy in large vessels (SSIM: 0.97 before denoising vs. 0.98 after denoising), but also substantially improves the accuracy in microvessels (SSIM: 0.74 before vs. 0.93 after). For the flow speed measurement, the denoising significantly improves the accuracy in both large vessels (SSIM: 0.83 before vs. 0.94 after) and microvessels (SSIM: 0.78 before vs. 0.93 after).

To test if this denoising technique permits a more aggressive relaxation of the fluence, we further reduced the pulse energy to 10% and 5% of the normal fluence level (*i.e.*, 10 and 5 nJ). As shown in Fig. 8a and quantified in Table II, the two-step denoising respectively improves the SNR values of large vessels and microvessels by 5.3 and 3.9 times at 10% of the normal fluence, and by 4.2 and 2.4 times at 5% of the normal fluence. Similarly, after denoising, a significant enhancement in the CNR is observed in the images acquired with 10% (5.9)

and 9.4 times in large vessels and microvessels, respectively) and 5% (4.9 and 9.0 times in large vessels and microvessels, respectively) of the normal fluence. Although the image quality is significantly improved, the SSIM of microvascular structure between the denoised low-fluence images and reference image acquired with 100 nJ pulses remains considerably low (0.83 and 0.65 at 10% and 5% of the normal fluence, respectively, as shown in Table II), which indicates only a partial retrieval of microvascular visualization. Similarly, this denoising technique improves the accuracy of the multi-parametric quantification. However, some SSIM values of the C_{Hb}, sO₂, and flow speed measurements remain lower than 0.9 after denoising (as shown in Table III), implying that considerable errors still exist (also seen in Fig. 8b–d, respectively).

With the aid of vessel segmentation, the measurement errors are quantified for the raw and denoised C_{Hb}, sO₂, and blood flow

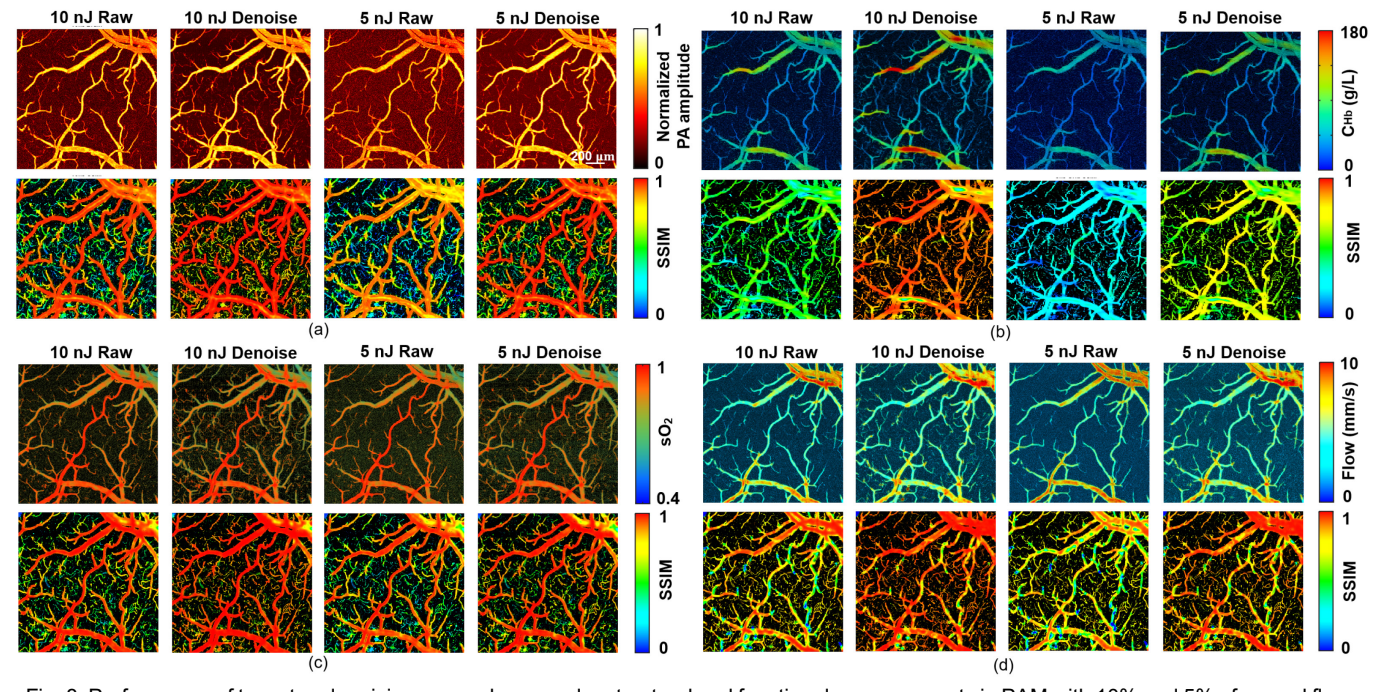


Fig. 8. Performance of two-step denoising on cerebrovascular structural and functional measurements in PAM with 10% and 5% of normal fluence (*i.e.*, 10 and 5 nJ pulse energy, respectively). (a) Raw and denoised cerebrovascular structural images acquired with 10 nJ and 5 nJ pulse energy, and their SSIM maps against the reference image acquired with normal fluence (*i.e.*, 100 nJ). (b) Raw and denoised C_{Hb} images acquired with 10 nJ and 5 nJ pulse energy, and their SSIM maps against the reference image acquired with normal fluence. (c) Raw and denoised sO_2 images acquired with 10 nJ and 5 nJ pulse energy, and their SSIM maps against the reference image acquired with normal fluence. (d) Raw and denoised blood flow images acquired with 10 nJ and 5 nJ pulse energy, and their SSIM maps against the reference image acquired with normal fluence. PA: photoacoustic.

TABLE IV	
RELATIVE ERRORS (AGAINST 100 NJ) IN QUANTITATIVE MEASUREMENTS OF CEREBROVASCULAR FUNCTION BEFORE AND AFTER DENOISIN	G

Functional	20	nJ	10	nJ	5 nJ		
Parameter ^a	Raw	Denoise	Raw	Denoise	Raw	Denoise	
C_{Hb}	20.1±4.7%	4.9±3.2%	50.0±3.9%	24.1±3.9%	69.9±2.8%	49.3±3.2%	
sO_2	2.1±1.4%	$2.0\pm1.4\%$	2.5±2.6%	2.3±2.7%	3.6±3.4%	3.1±3.7%	
Flow	10.0±5.6%	3.2±2.4%	9.9±6.8%	$4.4\pm2.9\%$	9.8±5.5%	5.3±3.3%	

^aParameters are measured in the 15 vessel segments shown in Supplementary Materials. Results are presented as mean ± standard deviation.

images acquired at different fluence levels against the reference images acquired with the normal fluence. As shown in Table IV, before denoising, the low-fluence images present considerable errors in the C_{Hb} and blood flow measurements and relatively small errors in the sO₂ measurement. At 20% of the normal fluence, the errors in C_{Hb}, sO₂, and blood flow measurements are 20.1%, 2.1%, and 10.0% before denoising and are reduced to 4.9%, 2.0%, and 3.2% after denoising, respectively. At even lower laser fluence levels, the denoising can still improve the quantitative accuracy, but the measurement errors remain considerably high after denoising. At 10% of the normal fluence, the denoising reduces the relative errors in C_{Hb}, sO₂, and flow measurements from 50.0%, 2.5%, and 9.9% to 24.1%, 2.3%, and 4.4%, respectively. At 5% of the normal fluence, the denoising reduces the relative errors in C_{Hb}, sO₂, and flow measurements from 69.9%, 3.6%, and 9.8% to 49.3%, 3.1%, and 5.3%, respectively.

IV. CONCLUSION AND DISCUSSION

In conclusion, we have developed a sparse coding-based twostep technique to improve the image quality and quantitative accuracy of low-fluence multi-parametric PAM. In an intravital brain imaging setting, we show that sequential sparse coding of the B-scans and the MAP image significantly removes the noise that accompanies the vascular signals in individual A-lines and that presents as the background fluctuation in the MAP image.

Functional quantification of C_{Hb}, sO₂, and blood flow speed is achieved by statistical, spectroscopic and correlation analysis of PAM data, respectively [7]. As shown by our previous study [15], if the photoacoustic signal is contaminated by noise, its amplitude and standard deviation, as well as the correlation of sequentially acquired A-lines, will all be affected, resulting in inaccurate quantification of these functional parameters. Effectively removing the noise while maximally preserving the amplitude and profile of the signal in low-fluence PAM images, this denoising technique offers not only improved visualization of the microvascular structure but also enhanced measurement accuracy of the microvascular function, including C_{Hb}, sO₂, and blood flow.

As an unsupervised learning strategy, the sparse codingbased denoising technique does not require a ground truth. Compared to supervised learning-based approaches [33], this technique is applicable in situations where the ground truth is not available.

Although demonstrated in the setting of low-fluence multiparametric PAM, the sparse coding-based two-step denoising technique is not specific to noise type or source. It is applicable to other photoacoustic imaging systems, including high-speed PAM and deep-penetration photoacoustic tomography, where improved image quality is highly desired but often difficult to achieve due to the tight photon budget.

The reported technique has a limitation that warrants further development. Implemented in a serial computing scheme, this technique processes B-scans one by one and is time-consuming (~3 hours for the *in vivo* brain dataset). Using the MATLAB Parallel Computing Toolbox to process B-scans in parallel can reduce the runtime by 45% (with four parallel workers). Future implementation using a dedicated GPU is expected to further reduce the processing time.

ACKNOWLEDGMENT

The authors thank Dr. Naidi Sun for assistance on generating the multi-parametric PAM images of the mouse brain. Also, Zhuoying Wang thanks Washington University in St. Louis for providing the Imaging Sciences Pathway Fellowship to support her doctoral research.

REFERENCES

- [1] K. Maslov, H. F. Zhang, S. Hu, and L. V. Wang, "Optical-resolution photoacoustic microscopy for in vivo imaging of single capillaries," *Opt. Lett.*, vol. 33, no. 9, pp. 929–931, May 2008, doi: 10.1364/OL.33.000929.
- [2] L. V. Wang and S. Hu, "Photoacoustic Tomography: In Vivo Imaging from Organelles to Organs," *Science*, vol. 335, no. 6075, pp. 1458– 1462, Mar. 2012, doi: 10.1126/science.1216210.
- [3] S. Hu and L. V. Wang, "Photoacoustic imaging and characterization of the microvasculature," *J. Biomed. Opt.*, vol. 15, no. 1, p. 011101, Feb. 2010, doi: 10.1117/1.3281673.
- [4] P. Beard, "Biomedical photoacoustic imaging," *Interface Focus*, vol. 1, no. 4, Art. no. 4, Aug. 2011, doi: 10.1098/rsfs.2011.0028.
- [5] S. V. Ovsepian, I. Olefir, G. Westmeyer, D. Razansky, and V. Ntziachristos, "Pushing the Boundaries of Neuroimaging with Optoacoustics," *Neuron*, vol. 96, no. 5, pp. 966–988, Dec. 2017, doi: 10.1016/j.neuron.2017.10.022.
- [6] B. Ning et al., "Simultaneous photoacoustic microscopy of microvascular anatomy, oxygen saturation, and blood flow," Opt. Lett., vol. 40, no. 6, pp. 910–913, Mar. 2015, doi: 10.1364/OL.40.000910.
- [7] B. Ning et al., "Ultrasound-aided Multi-parametric Photoacoustic Microscopy of the Mouse Brain," Sci. Rep., vol. 5, p. 18775, Dec. 2015, doi: 10.1038/srep18775.
- [8] T. Wang et al., "Multiparametric photoacoustic microscopy of the mouse brain with 300-kHz A-line rate," *Neurophotonics*, vol. 3, no. 4, p. 045006, Nov. 2016, doi: 10.1117/1.NPh.3.4.045006.
- [9] F. Zhong et al., "High-speed wide-field multi-parametric photoacoustic microscopy," Opt. Lett., vol. 45, no. 10, pp. 2756–2759, May 2020, doi: 10.1364/OL.391824.
- [10] J. Yao et al., "High-speed Label-free Functional Photoacoustic Microscopy of Mouse Brain in Action," Nat. Methods, vol. 12, no. 5, pp. 407–410, May 2015, doi: 10.1038/nmeth.3336.

- [11] Mohesh Moothanchery, Renzhe Bi, Jin Young Kim, Ghayathri Balasundaram, Chulhong Kim, and Malini C. Olivo, "High-speed simultaneous multiscale photoacoustic microscopy," *J. Biomed. Opt.*, vol. 24, no. 8, Art. no. 8, Aug. 2019, doi: 10.1117/1.JBO.24.8.086001.
- [12] L. V. Wang and J. Yao, "A practical guide to photoacoustic tomography in the life sciences," *Nat. Methods*, vol. 13, no. 8, pp. 627–638, Aug. 2016, doi: 10.1038/nmeth.3925.
- [13] A. Danielli, K. Maslov, C. P. Favazza, J. Xia, and L. V. Wang, "Nonlinear photoacoustic spectroscopy of hemoglobin," *Appl. Phys. Lett.*, vol. 106, no. 20, May 2015, doi: 10.1063/1.4921474.
- [14] J. Yao and L. V. Wang, "Sensitivity of photoacoustic microscopy," *Photoacoustics*, vol. 2, no. 2, Art. no. 2, Apr. 2014, doi: 10.1016/j.pacs.2014.04.002.
- [15] Z. Xu, N. Sun, R. Cao, Z. Li, Q. Liu, and S. Hu, "Cortex-wide multiparametric photoacoustic microscopy based on real-time contour scanning," *Neurophotonics*, vol. 6, no. 3, Jul. 2019, doi: 10.1117/1.NPh.6.3.035012.
- [16] G. Guney, N. Uluc, A. Demirkiran, E. Aytac-Kipergil, M. B. Unlu, and O. Birgul, "Comparison of noise reduction methods in photoacoustic microscopy," *Comput. Biol. Med.*, vol. 109, pp. 333–341, Jun. 2019, doi: 10.1016/j.compbiomed.2019.04.035.
- [17] A. Longo, S. Morscher, J. M. Najafababdi, D. Jüstel, C. Zakian, and V. Ntziachristos, "Assessment of hessian-based Frangi vesselness filter in optoacoustic imaging," *Photoacoustics*, vol. 20, p. 100200, Dec. 2020, doi: 10.1016/j.pacs.2020.100200.
- [18] S. H. Holan and J. A. Viator, "Automated wavelet denoising of photoacoustic signals for circulating melanoma cell detection and burn image reconstruction," *Phys. Med. Biol.*, vol. 53, no. 12, Art. no. 12, May 2008, doi: 10.1088/0031-9155/53/12/n01.
- [19] I. Ul Haq, R. Nagaoka, S. Siregar, and Y. Saijo, "Sparse-representation-based denoising of photoacoustic images," *Biomed. Phys. Eng. Express*, vol. 3, no. 4, Art. no. 4, Jul. 2017, doi: 10.1088/2057-1976/aa7a44.
- [20] P. Farnia et al., "Dictionary learning technique enhances signal in LED-based photoacoustic imaging," Biomed. Opt. Express, vol. 11, no. 5, Art. no. 5, May 2020, doi: 10.1364/BOE.387364.
- [21] S. Govinahallisathyanarayana, B. Ning, R. Cao, S. Hu, and J. A. Hossack, "Dictionary learning-based reverberation removal enables depth-resolved photoacoustic microscopy of cortical microvasculature in the mouse brain," *Sci. Rep.*, vol. 8, no. 1, p. 985, 17 2018, doi: 10.1038/s41598-017-18860-3.
- [22] H. Chen, B. Jiang, and W. Chen, "Image super-resolution based on patches structure," in 2011 4th International Congress on Image and Signal Processing, Oct. 2011, vol. 2, pp. 1076–1080. doi: 10.1109/CISP.2011.6100283.
- [23] J. Yang, J. Wright, T. S. Huang, and Y. Ma, "Image Super-Resolution Via Sparse Representation," *IEEE Trans. Image Process.*, vol. 19, no. 11, Art. no. 11, Nov. 2010, doi: 10.1109/TIP.2010.2050625.
- [24] M. Elad and M. Aharon, "Image Denoising Via Sparse and Redundant Representations Over Learned Dictionaries," *IEEE Trans. Image Process.*, vol. 15, no. 12, Art. no. 12, Dec. 2006, doi: 10.1109/TIP.2006.881969.
- [25] M. Aharon, M. Elad, and A. Bruckstein, "K-SVD: An algorithm for designing overcomplete dictionaries for sparse representation," *IEEE Trans. Signal Process.*, vol. 54, no. 11, Art. no. 11, Nov. 2006, doi: 10.1109/TSP.2006.881199.
- [26] H. Zhao et al., "Deep Learning Enables Superior Photoacoustic Imaging at Ultralow Laser Dosages," Adv. Sci. Weinh. Baden-Wurtt. Ger., vol. 8, no. 3, pp. 2003097–2003097, Dec. 2020, doi: 10.1002/advs.202003097.
- [27] J. Mairal, M. Elad, and G. Sapiro, "Sparse Representation for Color Image Restoration," *IEEE Trans. Image Process.*, vol. 17, no. 1, pp. 53–69, Jan. 2008, doi: 10.1109/TIP.2007.911828.
- [28] M. Aharon, M. Elad, and A. Bruckstein, "K-SVD: An algorithm for designing overcomplete dictionaries for sparse representation," *IEEE Trans. Signal Process.*, vol. 54, no. 11, pp. 4311–4322, Nov. 2006, doi: 10.1109/TSP.2006.881199.
- [29] Y. C. Pati, R. Rezaiifar, and P. S. Krishnaprasad, "Orthogonal matching pursuit: recursive function approximation with applications to wavelet decomposition," in *Proceedings of 27th Asilomar Conference on Signals, Systems and Computers*, Nov. 1993, pp. 40–44 vol.1. doi: 10.1109/ACSSC.1993.342465.
- [30] P. Hajireza, A. Forbrich, and R. Zemp, "In-Vivo functional opticalresolution photoacoustic microscopy with stimulated Raman scattering

- fiber-laser source," *Biomed. Opt. Express*, vol. 5, no. 2, Art. no. 2, Feb. 2014, doi: 10.1364/BOE.5.000539.
- [31] L. V. Wang and H. Wu, Biomedical optics: principles and imaging. New Jersey: John Wiley, 2007.
- Zhou Wang, A. C. Bovik, H. R. Sheikh, and E. P. Simoncelli, "Image quality assessment: from error visibility to structural similarity," *IEEE Trans. Image Process.*, vol. 13, no. 4, pp. 600–612, Apr. 2004, doi: 10.1109/TIP.2003.819861.
- [33] K. Zhang, W. Zuo, Y. Chen, D. Meng, and L. Zhang, "Beyond a Gaussian Denoiser: Residual Learning of Deep CNN for Image Denoising," *IEEE Trans. Image Process.*, vol. 26, no. 7, pp. 3142–3155, Jul. 2017, doi: 10.1109/TIP.2017.2662206.